



Corrosion Behavior of Harmonic Structured 316L Stainless Steel in 3.5% NaCl and Simulated Body Fluid Solution

Prabhat K. Rai, S. Shekhar, K. Yagi, K. Ameyama, and K. Mondal

(Submitted July 6, 2019; published online December 3, 2019)

Corrosion behavior of a 316L stainless steel with harmonic microstructure was studied and compared with a sintered non-harmonic and a conventional (wrought) 316L stainless steel in 3.5% NaCl and Hanks' solution. The study was performed using linear polarization, dynamic polarization and electrochemical impedance spectroscopy. The harmonic, conventional and non-harmonic 316L stainless steels showed similar corrosion resistance in both the solutions. However, the harmonic steel showed better passivation behavior as compared to that of the wrought and sintered non-harmonic steel. Harmonically distributed fine grains and higher twin boundary fraction were attributed to the improvement in its passivation behavior.

Keywords corrosion, harmonic structure, polarization

1. Introduction

Biomaterials play significant role in the life of human beings as they are widely used for the manufacturing of artificial replacements in human bodies for the proper functioning of vital organs (Ref 1). Outstanding corrosion resistance, biocompatibility and good mechanical strength make 316L stainless steel attractive to be used in surgical implants (Ref 2). Moreover, 316L stainless steel is also used in automotive components and high-pressure vessels (Ref 3). If the properties are further improved, its applications can be broadened, and life of the components made out of it can be enhanced. The properties of the materials can be upgraded either by modifying the chemical composition or by modifying their microstructure. The pioneer work of Hall (Ref 4) and Petch (Ref 5) has paved the way of microstructural route through grain refinement. The strength has been found to increase with grain refinement in case of the 316L stainless steel too (Ref 6). The remarkable improvement in the strength has been achieved by reducing the grain size to nano-crystalline (NC)/ultra-fine grains (UFG) regime in 316L stainless steel, but at the cost of ductility owing to premature appearance of the plastic instability (Ref 7, 8). For improving the ductility in the NC/UFG materials, harmonic structure consisting of periodically distributed coarse and fine grains has been introduced by Prof. Ameyama and his group (Ref 3, 9). In contrast to the conventional bimodal microstructure,

harmonic structure design has been found to restrict the strain localization, which would lead to an optimum combination of strength and ductility (Ref 3). Though harmonic structure design can make the materials strong as well as ductile, its corrosion behavior must be studied in detail before using the harmonic structured materials in real life applications. Despite having good mechanical properties, poor corrosion resistance leads to shorter life of the material.

Importance of grain size/grain boundaries cannot be overlooked in the study of corrosion behavior of any material because grain boundaries usually act as vulnerable sites in the material (Ref 10). Corrosion behavior of materials with refined grains has been investigated in detail, but the reported results are not consistent (Ref 11). It has been noted that in some materials, corrosion performance deteriorates due to reduction in grain size and subsequent increased number of reactive sites (grain boundaries) (Ref 12, 13), whereas some materials display enhanced resistance against corrosion with decrease in grain size owing to improved passivation tendency (Ref 14, 15).

Lü et al. (Ref 16) have studied the effect of fine grains and mechanical twins on the corrosion behavior of a 316L grade of stainless steel in 0.05 M H₂SO₄ + 0.25 M Na₂SO₄ and found that corrosion resistance improves for the sample with numerous twins, whereas it decreases in case of nano-crystalline grains (~ 60 nm) due to the improper compactness of the oxide film as compared to its counterpart with relatively coarser grains. Niu et al. (Ref 17) have reported that the corrosion performance of bimodal ferrite steel in 5% NaCl solution is superior to that of its parent dual phase steel due to relatively smaller potential difference measured by scanning Kelvin probe force microscopy in bimodal ferrite steel, which is favorable for better protective rust formation. Corrosion properties of a 304L stainless steel with harmonic microstructure have been studied in 3.5% NaCl solution by our group (Ref 18), and improved corrosion resistance has been found by harmonic structure design. It has been observed that fine-grained region (shell) experiences preferential dissolution, whereas coarse-grained region (core) undergoes very little corrosion. The above-mentioned study has been found to be the single report on the

Prabhat K. Rai, S. Shekhar, and K. Mondal, Department of Materials Science and Engineering, Indian Institute of Technology Kanpur, Kanpur, UP 208016, India; **K. Yagi**, Graduate School of Science and Engineering, Ritsumeikan University, Kusatsu, Shiga 5258577, Japan; **K. Ameyama**, Faculty of Science and Engineering, Ritsumeikan University, Kusatsu, Shiga 5258577, Japan. Contact e-mail: prabhatrai2008@gmail.com.

corrosion behavior of materials with harmonic microstructure to the best of authors' knowledge. Hence, a detailed investigation is still warranted to understand the corrosion behavior of the harmonic structured materials.

In this work, a 316L stainless steel has been chosen for preparing sintered samples with harmonic and non-harmonic microstructures. The earlier work by Ameyama et al. (Ref 3, 9) on harmonic structured 316L stainless steel shows better mechanical properties (higher strength as well as higher ductility). Therefore, it is interesting to study its corrosion behavior in both NaCl and Hanks' solution, since 316L steel finds wide application as biomaterials. Since the new harmonic microstructure is unique in its mechanical (Ref 3, 9) as well as wear behavior (Ref 19, 20), our primary interest is to see the relative corrosion behavior of the 316L with conventional and harmonic microstructures on the basis of linear and dynamic polarization. Hence, it is an interrelation between the physical metallurgy with the polarization behavior of the three microstructures of 316L steel. These samples with different microstructures have been subjected to electrochemical tests, which consist of linear and dynamic polarization as well as impedance spectroscopic analysis in 3.5% NaCl and Hanks' simulated body fluid solutions. The electrochemical behavior of the harmonic and non-harmonic 316L samples has been then compared with a wrought conventional 316L stainless steel of similar composition. Finally, the relative corrosion behavior of the three steels has been analyzed and discussed with reference to their response to the electrochemical tests and typical microstructures.

2. Materials and Methods

The chemical composition of the initial 316L stainless steel powder is presented in Table 1. Mechanical milling was conducted using planetary ball mill (Fritch P-5) with 304 stainless steel vial and balls of diameter 5 mm in the atmosphere of argon gas at ambient temperature. The ball-to-powder weight ratio was kept at 2:1, and the resulting mixture was subjected to milling for 50 h at 200 rpm. Afterward, powders (milled and un-milled) were sintered using spark plasma sintering (LABOX-675, NJS) for 3600 s at the temperature and pressure of 1223 K and 50 MPa, respectively, in the vacuum of < 15 Pa. Sintering of milled and un-milled powders resulted in the development of harmonic and non-harmonic microstructures, respectively. The chemical composition of a conventional (wrought) 316L stainless steel is also listed in Table 1. Hardness values were estimated using a hardness tester (Bareiss Prüfgerätebau GmbH) at 100 g load. The dwell time was 10 s.

For microstructural characterization, the samples were ground on silicon carbide emery papers (up to 1200 grit size)

and subsequently cloth polishing was carried out using a solution containing 1 μm particle size of alumina with the help of a polishing machine (Buehler) operating at 600 rpm. After cleaning with water, samples were dried in warm air and thereafter, ultrasonic cleaning was done in acetone. The harmonic and non-harmonic 316L stainless steel samples were etched using a solution containing 10 mL perchloric acid and 90 mL ethanol, whereas the conventional 316L stainless steel samples were etched with 80 mL HCl and 20 mL HNO_3 solution. Microstructures were investigated using an optical microscope (Carl Zeiss). Average grain size was obtained with the help of ImageJ software stereologically (linear intercept method). Volume fractions of shell and core regions were determined stereologically (point counting method) using ImageJ software. Minimum five micrographs were selected for stereological calculations. Phases present in the microstructure were identified with the help of x-ray diffraction (Panalytical Empyrean) operating with $\text{CuK}\alpha$ radiation ($\lambda = 1.54 \text{ \AA}$), and the range of scanning angle ($2\theta, ^\circ$) was $30^\circ\text{--}90^\circ$.

Electron backscattered diffraction (EBSD) analysis was carried out using a field emission scanning electron microscope (JEOL JSM-7100F) with Oxford Channel 5 EBSD attachment. The samples were prepared by electropolishing in an electrolyte containing 412 mL methanol, 247 mL 2-butoxyethanol and 41 mL perchloric acid at 35 V for 13 s. Multiple areas of size $380 \times 280 \mu\text{m}^2$ at the random locations of the samples were scanned. The step size and binning mode were 0.5 μm and 4×4 , respectively. AZtecHKL EBSD software was used for estimating length of high-angle grain boundaries (HAGBs/area) and twin boundaries/area.

The samples for electrochemical tests were prepared according to ASTM G5-14 (Ref 21). After polishing, the samples were washed with water and cleaned by ultrasonating in acetone. Electrochemical experiments were conducted with the help of a PARSTAT 2263 (Princeton Applied Research) potentiostat using a standard flat bottom cell by exposing 1 cm^2 area of the sample. Counter and reference electrodes were platinum wire mesh and a saturated calomel electrode ($E_{\text{SCE}} = +241 \text{ mV}_{\text{SCE}}$), respectively. The experiments were conducted in a freely aerated 3.5% NaCl solution and Hanks' simulated body fluid solution at room temperature. The Hanks' solution has been prepared by mixing NaCl (8 g/L), KCl (0.4 g/L), CaCl_2 (0.14 g/L), NaHCO_3 (0.35 g/L), $\text{Na}_2\text{HPO}_4 \cdot 2\text{H}_2\text{O}$ (0.06 g/L), KH_2PO_4 (0.6 g/L), $\text{MgSO}_4 \cdot 7\text{H}_2\text{O}$ (0.06 g/L), $\text{MgCl}_2 \cdot 6\text{H}_2\text{O}$ (0.1 g/L) and glucose (1.0 g/L) (Ref 22). The pH of the Hanks' solution was measured to be 7.4.

Steady-state values of open-circuit potential (OCP) were recorded after immersing the samples in the electrolytes for 2 h. Linear and dynamic polarization experiments were conducted at a standard scan rate of 0.166 mV/s in 3.5% NaCl and Hanks' simulated body fluid solutions. Electrochemical impedance spectroscopy (EIS) was conducted at OCP with sinusoidal AC amplitude of 10 mV within the frequency range of 100 kHz–

Table 1 Chemical composition of harmonic and conventional 316L stainless steels

Steel	C	Si	Mn	P	S	Ni	Cr	Mo	Fe
HS 316L SS	0.018	0.9	1.07	0.032	0.017	12.4	17.3	2.1	Bal.
Conv. 316L SS	0.02	0.34	1.8	0.01	0.01	11.2	18.3	2.1	Bal.

The sintered non-harmonic 316L stainless steel has the same composition as the harmonic steel

10 mHz. Data points were modeled using ZSimpwin software (version 3.21) and fitted with the help of equivalent electrical circuits. Multiple tests were conducted to check the reproducibility of the obtained results. The samples were characterized after performing electrochemical tests using a Tungsten scanning electron microscope (Jeol, JSM-6010LA). The passive films formed during dynamic polarization tests were analyzed with the help of Acton SpectraPro SP-2500 Raman spectrometer using excitation laser of 532 nm wavelength coupled with Olympus optical microscope.

3. Results and Discussion

The optical micrographs of the harmonic 316L stainless steel are shown in Fig. 1(a) (low magnification) and (b) (high magnification). It is clear from Fig. 1(a) and (b) that the microstructure is heterogeneous in nature and it consists of bimodal grains. It can be noticed that coarser grains (core) are enclosed by interconnected network of fine grains (shell). This distribution of fine and coarse grains is almost uniform throughout the material. The grain size has been determined to be $5 \pm 1 \mu\text{m}$ in the shell region, whereas $18 \pm 4 \mu\text{m}$ in the core region. Volume fractions of the core and shell regions were estimated to be ~ 61 and $\sim 39\%$, respectively. The above-mentioned microstructure is similar to the harmonic structure reported in the literature for different materials (Ref 19, 23). Microstructures of the conventional (Fig. 1c) and sintered non-harmonic (Fig. 1d) 316 stainless steel consist of grains of average grain size 28 ± 4 and $26 \pm 5 \mu\text{m}$, respectively. In order to identify the phases, x-ray diffraction analysis has been

performed (Fig. 2). The peaks of austenite were found in case of all the three 316L stainless steel samples.

Figures 3(a), (b) and (c) show the EBSD micrographs of the harmonic, conventional and non-harmonic 316L stainless steel samples, respectively. Lines in green and black colors show low-angle (misorientation angle 5° – 15°) and high-angle grain boundaries (misorientation angle $> 15^\circ$), whereas lines in red color show the twin boundaries. Unindexed points are marked by black spots. The grain size distribution (plotted at the same scale) is shown in Fig. 4(a), (b) and (c) for the harmonic, conventional, non-harmonic 316L stainless steel samples, respectively. It is clear from Fig. 4(a), (b) and (c) that the fraction of finer grains ($< 10 \mu\text{m}$) in the harmonic 316L stainless steel sample is the highest among all the three samples. This can be due to the presence of fine grains (shell) in the microstructure of the harmonic 316L stainless steel. It can also be noticed that grains with average grain size larger than $20 \mu\text{m}$ are present in significant number in the microstructure of conventional (Fig. 4b) and sintered non-harmonic (Fig. 4c) 316L stainless steels, whereas fraction of grains $> 20 \mu\text{m}$ is almost negligible in the harmonic structured stainless steel sample (Fig. 4a).

Lengths of HAGB/area and twin boundaries/area have been estimated from the EBSD micrographs for all the three samples and shown in Fig. 5(a) and (b). It is clear from Fig. 5(a) that length of HAGBs/area in the harmonic stainless steel sample is approximately double as compared to that in the conventional and sintered non-harmonic stainless steel samples. This can be due to the presence of huge number of finer grains in the harmonic 316L stainless steel. Length of twin boundaries/area is also maximum in the harmonic stainless steel sample among all the three steel samples as illustrated in Fig. 5(b).

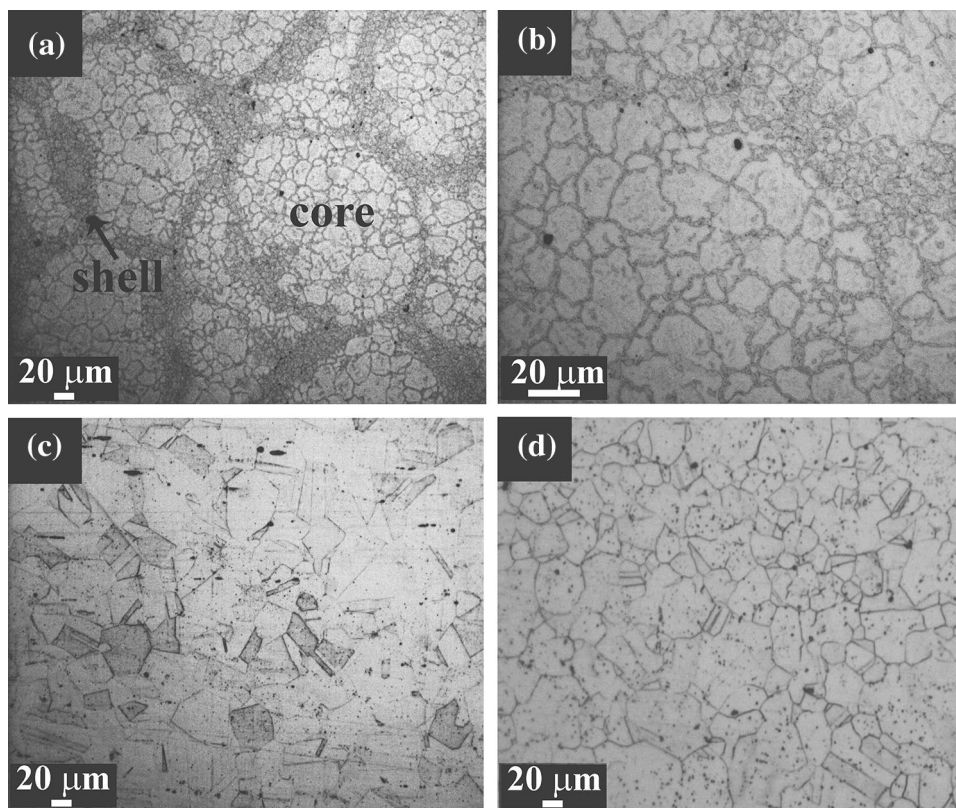


Fig. 1 Optical micrographs of (a) and (b) harmonic (c) conventional and (d) non-harmonic 316L stainless steel samples

The hardness values of shell and core regions of harmonic steel were estimated to be 219 ± 17 and 196 ± 8 , respectively, whereas those of conventional and sintered non-harmonic 316L stainless steel were measured to be 223 ± 11 and 186 ± 10 , respectively. Hardness is higher for shell region of harmonic 316L stainless steel than that of core which can be due to finer grains present in the shell region. In addition to the hardness, Zheng et al. (Ref 3) have reported that a good combination of strength ($\sigma_y = 695$ MPa) and ductility ($\epsilon_u = 27.1\%$) has been achieved by harmonic structure design in SUS316L stainless steel.

Linear polarization experiments were conducted in 3.5% NaCl solution with the samples of the harmonic, conventional and the non-harmonic 316L stainless steels as shown in Fig. 6(a). The polarization resistance (R_p) can be estimated by determining the slope of the linear polarization plot at zero over-potential given by Eq 1 according to ASTM standard G102-89 (Ref 24)

$$\text{Polarization resistance}(R_p) = (\Delta E / \Delta i) \quad (\text{Eq 1})$$

The polarization resistance (R_p) values are listed in Table 2. It can be noticed in Fig. 6(a) that the slope for the harmonic 316L stainless steel is markedly higher than the slope for the sintered non-harmonic stainless steel sample. The slope of the

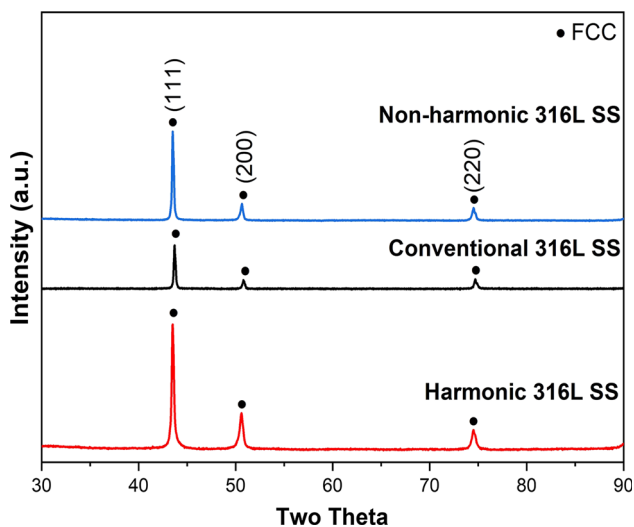


Fig. 2 X-ray diffraction plots of harmonic, conventional and non-harmonic structured 316L stainless steel samples

linear polarization plot (Fig. 6a) for the harmonic steel sample is similar to the slope of conventional 316L stainless steel sample. This attributes to interconnected finer grains around the coarse grains leading to uniform distribution of reactive zones in the harmonic steel.

Dynamic polarization tests were also conducted to understand the behavior of the harmonic 316L stainless steel in the wider potential range in 3.5% NaCl solution. The corrosion current density, i_{corr} , was estimated using Tafel extrapolation method, and the obtained values along with the values of β_a and β_c are listed in Table 2. The values of i_{corr} for the harmonic steel are close to those of the conventional 316L stainless steel and non-harmonic 316L stainless steel samples (Table 2). The improvement of corrosion resistance of a harmonic 304L stainless steel has been also reported in our earlier study (Ref 18). Lü et al. (Ref 16) and Trillo et al. (Ref 25) have suggested that twin ($\Sigma 3$) boundaries can decrease the corrosion sensitivity due to their significantly low interfacial free energy. It is obvious from Fig. 5(b) that length of twin boundaries per unit area in the harmonic 316L stainless steel is more than two times to that in the sintered non-harmonic 316L stainless steel. Better corrosion resistance in the harmonic 316L steel can be attributed to the higher fraction of twin boundaries.

A sudden increase in the current density can be noticed in the anodic branch of potentiodynamic plot of the harmonic and the conventional 316L stainless steel at 0.06 V (Fig. 6b). This behavior indicates that both the samples have tendency to passivate initially. But, the dissolution of the passive layer commences after reaching the potential value of 0.06 V. On the other hand, current density continuously increases in case of the sintered non-harmonic structured 316L stainless steels (Fig. 6b) which reflects that this sample does not have any tendency to passivate. Thus, it could be concluded that the harmonic and conventional stainless steel samples have displayed passivation tendency, whereas non-harmonic steel has not shown any signature of passivation (Fig. 6b). Moreover, the potential range in which passivation occurs are estimated to be 0.23 and 0.16 V for harmonic and conventional stainless steel samples, respectively. Hence, the breakdown potential for the harmonic and conventional steel is same, but the potential range in which passivation occurs is higher for the harmonic steel than that for the conventional one. Li et al. (Ref 26) have also shown the improvement of passivation ability of 316L stainless steel with nano-sized grains and nano-twins due to the development of Cr-enriched layer. The harmonic 316L stainless steel has large number of grain boundaries due to the presence of fine grains, whereas the grains are relatively coarser in the conventional

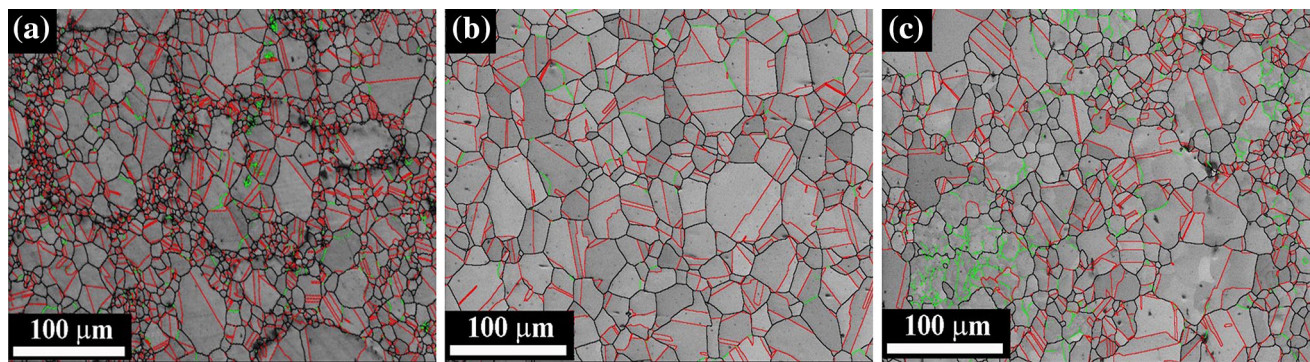


Fig. 3 EBSD micrographs of (a) harmonic (b) conventional and (c) non-harmonic 316L stainless steel samples

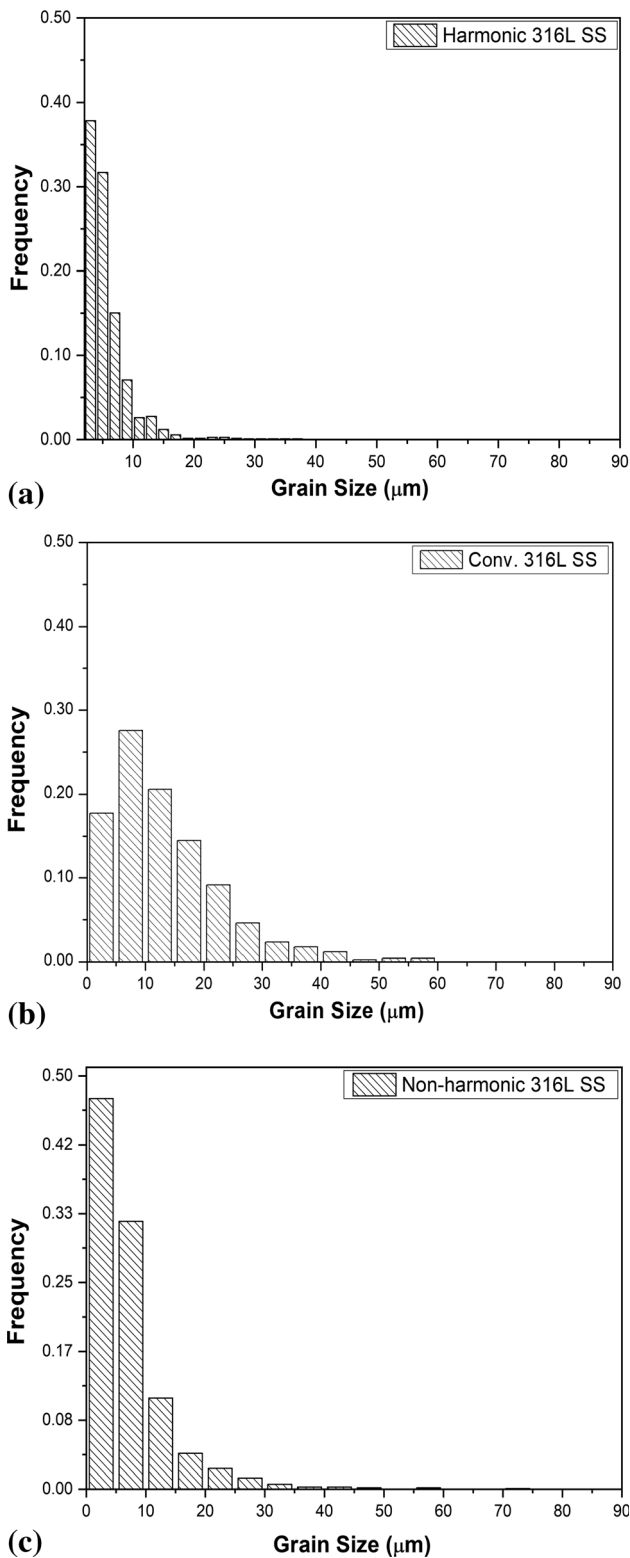


Fig. 4 Grain size distribution in (a) harmonic (b) conventional and (c) non-harmonic 316L stainless steel samples

steel. Though, the harmonic 316L steel contains higher twin boundary length per unit area than that in the conventional steel, HAGB length per unit area is lower in case of the conventional steel as compared to the harmonic steel. Hence, HAGB length per unit area and twin boundary length per unit

area act opposite to each other when corrosion behavior of both the steel is compared. Higher HAGB length per unit area increases the corrosion tendency in case of the harmonic steel, whereas higher twin boundary length per unit area tries to reduce the corrosion. Hence, the corrosion rates are counter-balanced in both the steels. On the other hand, the harmonic structured stainless steel consists of fine grains in the shell region and relatively more twins, and it can be attributed to enhanced passivation ability of the harmonic steel over other two steels with non-harmonic microstructures.

The difference in passivation behavior has been explained with the help of mixed potential theory as shown in Fig. 6(c). The cathodic branch of oxygen reduction reaction on harmonic 316L stainless steel surface intersects the passive region of anodic branch at lower potential as compared to that in the case of the conventional 316L steel. This has resulted in increase in the corrosion potential (E_{corr}) of the conventional 316L steel as compared to the harmonic steel, and the corrosion current density (i_{corr}) for the former becomes little less than that of the harmonic steel. Moreover, the passive region began earlier in case of the harmonic 316L steel as compared to the conventional 316L steel leading to higher passive region in the former as compared to latter. This plausibly happens because of the typical nature of anodic portions of the conventional steel (brown) and harmonic steel (blue).

Electrochemical impedance spectroscopy (EIS) has been carried out on all the three samples. The EIS data have been fitted and analyzed using the equivalent electrical circuit (inset of Fig. 6e), where R_s and R_c represent solution and charge transfer resistance. CPE is used to denote pseudo-double layer capacitance of the external porous layer for understanding the non-ideal characteristics of capacitive constant phase elements. Equation 2 (Ref 27) could be used to define the impedance of CPE (Z_{CPE})

$$Z_{CPE} = \frac{1}{Q(j\omega)^n} \quad (\text{Eq 2})$$

where Q proportionality constant ($\Omega^{-1} \text{ s}^n \text{ cm}^{-2}$), $j: \sqrt{-1}$, ω angular frequency ($\omega = 2\pi f$) and n factor indicating surface inhomogeneity ($-1 \leq n \leq 1$).

The capacitive, resistive and inductive behavior can be decided when n takes value of 1, 0 and -1 , respectively. Porous passive layer capacitance is indicated by the CPE_p , and R_f is the ionic resistance offered by the electrolyte present in the pore sections of the passive film. This equivalent circuit is typical of activation-controlled dissolution process. The polarization plots in Fig. 6(b) also show strong passivation behavior for the harmonic as well as conventional steels, whereas weak passivation has been observed in case of the non-harmonic stainless steel.

The values of different parameters obtained from the EIS data fitting are presented in Table 3 along with the Chi-squared values indicating goodness of fit. The diameter of semicircle in the Nyquist plot (Fig. 6d) gives the polarization resistance. It can be concluded from the polarization resistance values listed in Table 3 that the sample with the harmonic microstructure has the similar polarization resistance than that of the conventional and sintered non-harmonic 316L stainless steel. This observation is in accordance with the linear polarization results (Fig. 6a). Bode phase angle plot (Fig. 6e) shows that peak of the phase angle is similar for the harmonic, conventional and sintered non-harmonic 316L stainless steel showing a capac-

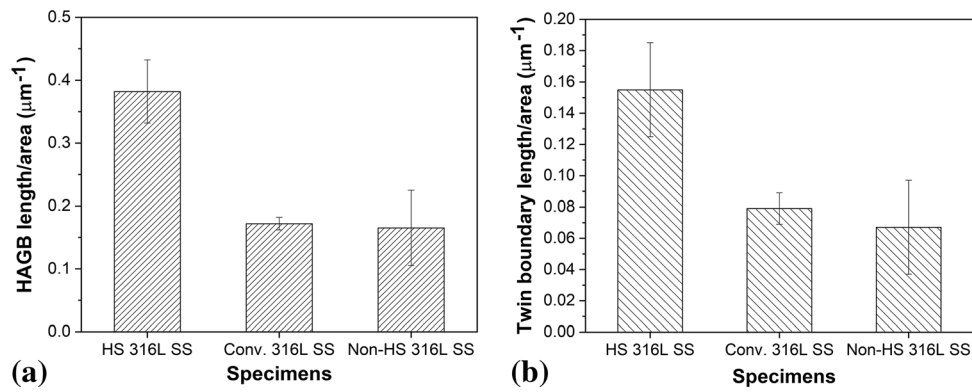


Fig. 5 Length of (a) high-angle grain boundaries and (b) twin boundaries per unit area in harmonic, conventional and non-harmonic 316L stainless steel samples

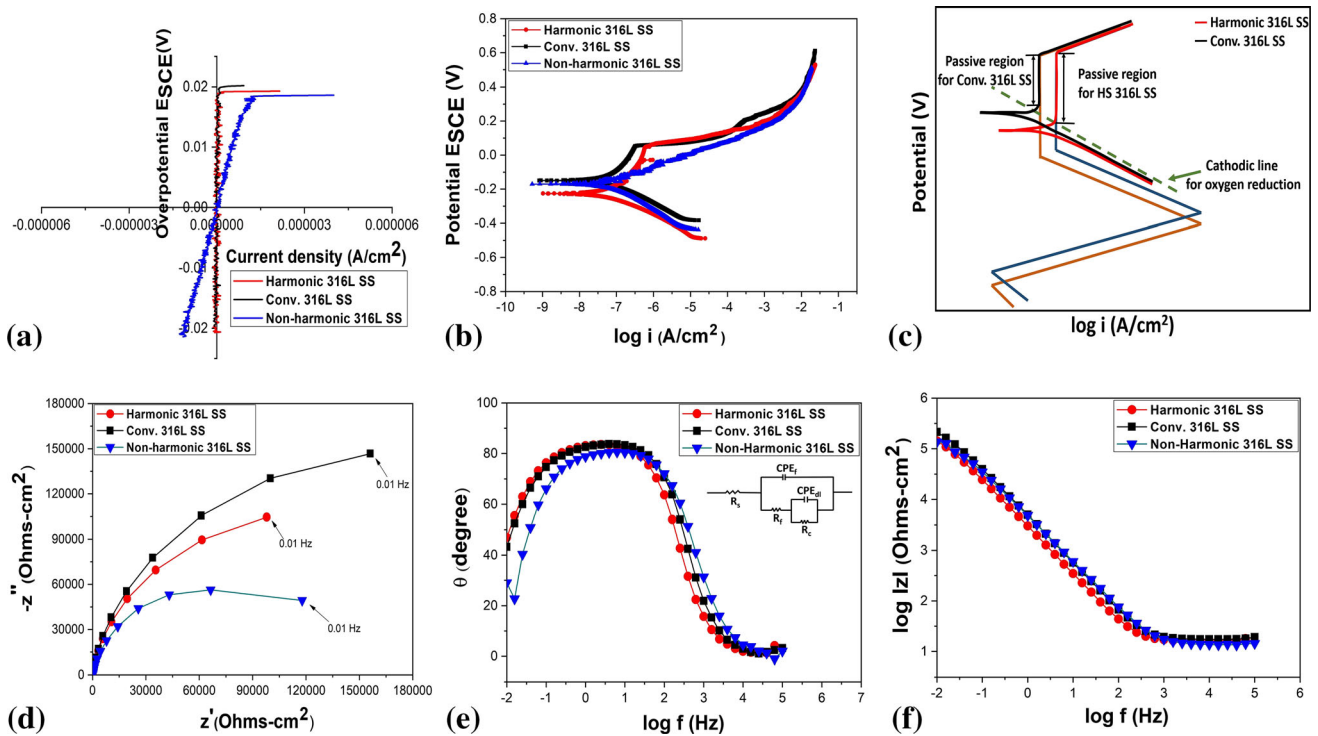


Fig. 6 (a) Linear polarization (b) dynamic polarization (c) schematic showing correlation with mixed potential theory (d) Nyquist plot (e) Bode phase angle plot and (f) Bode magnitude plot for harmonic, conventional and non-harmonic 316L stainless steel samples tested in 3.5% NaCl solution

Table 2 Values of electrochemical parameters obtained from electrochemical polarization in 3.5% NaCl solution

Material	$R_p, \Omega \text{ cm}^2$	$\beta_a, \text{mV/decade}$	$\beta_c, \text{mV/decade}$	$E_{\text{corr}}, \text{mV vs. SCE}$	$i_{\text{corr}}, \mu\text{A/cm}^2$
HS 316L SS	398202 ± 23716	261 ± 24	108 ± 21	-229 ± 17	0.079 ± 0.009
Conv. 316L SS	339210 ± 11264	346 ± 11	122 ± 17	-150 ± 12	0.065 ± 0.005
Non-HS 316L SS	157232 ± 16346	58 ± 14	122 ± 23	-171 ± 14	0.088 ± 0.003

itive behavior. However, low-frequency breakpoint at 10 mHz appears at lower phase angle in case of the sample with non-harmonic microstructure as compared to both the conventional and harmonic samples. Rather breakpoint at 10 mHz in case of the conventional and harmonic steels appears at almost same phase angle, suggesting stronger passive film formation as compared to the non-harmonic steel. The Bode magnitude plot

(Fig. 6f) also substantiates the similar polarization resistance of the harmonic, conventional and sintered non-harmonic 316L stainless steel.

In case of the 304L stainless steel, it has been seen that the shell region with relatively finer grains undergoes preferential corrosion as compared to insignificant corrosion of core with coarse grains (Ref 18). The similar behavior can also be noticed

Table 3 Data obtained from EIS measurements simulated using equivalent circuits in 3.5% NaCl solution

Specimen condition	HS 316L SS	Conv. 316L SS	Non-HS 316L SS
$R_s, \Omega \text{ cm}^2$	17	17.6	17
$R_f, \Omega \text{ cm}^2$	980	950	650
$CPE_f, \Omega^{-1} \text{ s}^n \text{ cm}^{-2} \times 10^{-5}$	3.6	3.1	2.0
n_1	0.95	0.96	1
$R_c, \Omega \text{ cm}^2$	3.6×10^5	3.8×10^5	1.6×10^5
$CPE_{dl}, \Omega^{-1} \text{ s}^n \text{ cm}^{-2} \times 10^{-6}$	5.5	7.8	19
n_2	0.43	0.64	0.79
χ^2 (Chi-squared)	1.6×10^{-3}	5.8×10^{-4}	1.6×10^{-2}

in the SEM micrograph of the harmonic 316L stainless steel samples after dynamic polarization tests (Fig. 7a). Numerous pits can be noticed in the SEM micrograph of the harmonic 316L stainless steel samples (Fig. 7a). It can be noticed in Fig. 7(a) that the pits are formed in a pattern which appears to be an interconnected network similar to the shell (fine grains) region. There is no pit in the inner region of the interconnected network which could be coarse-grained region. This could be due to the existence of two completely different grain size distributions in the harmonic structured steel. Owing to higher grain boundary fraction in the shell segment of the harmonic stainless steel, the corrosion is preferentially centered in the fine-grained regions leaving the coarse-grained segment uncorroded. In order to confirm the preferential dissolution of shell segment, the harmonic 316L steel sample has been polarized to a higher potential (0.8 V) and the corresponding SEM micrographs are shown in Fig. 8(a) and (b). It is clear the fine-grained (shell) regions of the harmonic steel have undergone severe preferential dissolution, whereas coarse-grained (core) regions have not corroded significantly. The presence of large number of reactive sites (grain boundaries) could have made the shell region more anodic with respect to core resulting in preferential corrosion of the shell segment in the harmonic steel.

The SEM micrograph of the conventional 316L stainless steel sample (Fig. 7b) shows some pits near the periphery of the area exposed to electrolyte as shown in the inset of Fig. 7(b). In contrast to this, the sintered non-harmonic 316L stainless steel sample (Fig. 7c) has undergone nominal corrosion.

To understand the stability of the harmonic 316L stainless steel in the human body, its corrosion behavior has also been studied in Hanks' solution (simulated body fluid). The linear polarization plots (Fig. 9a and Table 4) show that the polarization resistance of the sample with the harmonic structure is close (within the error limit) to that of the conventional and sintered non-harmonic 316L steel sample.

The dynamic polarization plots recorded for all the three samples in Hanks' solution are presented in Fig. 9(b). The values of corrosion current density (i_{corr}) (Table 4) also indicate that the corrosion resistance of the conventional and harmonic 316L steel samples is similar to that of the sintered non-harmonic 316L steel. The potentiodynamic plots of the conventional and harmonic 316L steels exhibit similar corrosion current densities and same values of breakdown potentials (~ 0.32 V). The breakdown potential for sintered non-harmonic 316L stainless steel is slightly lower than those for harmonic and conventional 316L steels. Gurappa et al. (Ref 22) have also reported the break down potential of the 316L stainless steel in Hanks' solution to be 0.28 V. The reason for

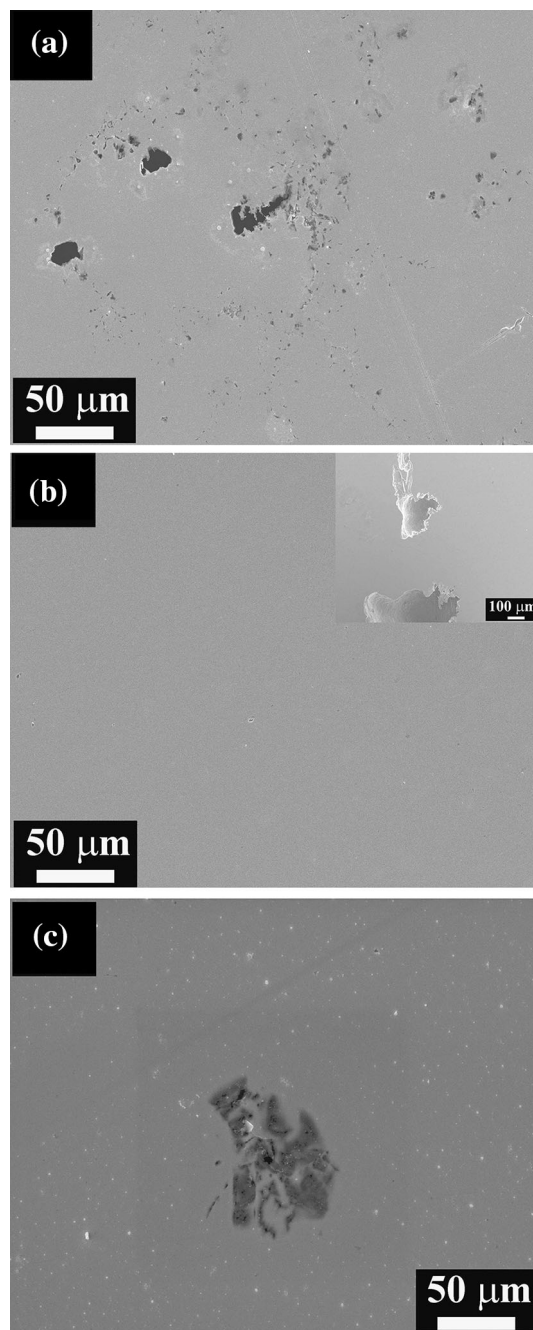


Fig. 7 SEM micrographs of (a) harmonic (b) conventional and (c) non-harmonic 316L stainless steel samples after dynamic polarization test in 3.5% NaCl solution

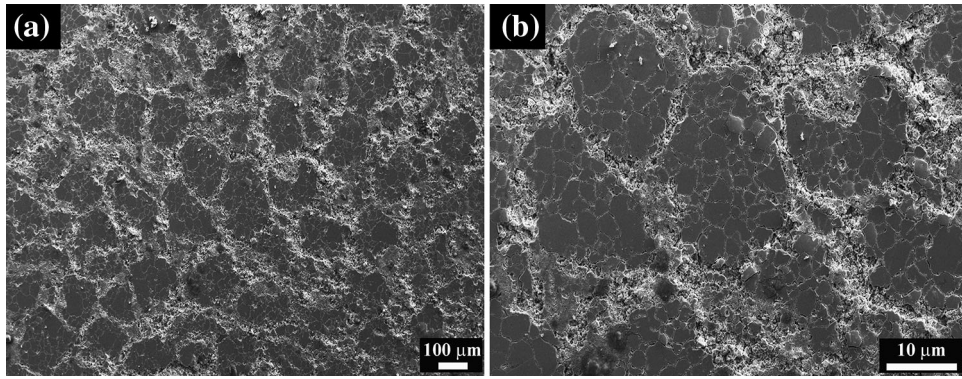


Fig. 8 (a) Low-magnification, (b) high-magnification SEM micrographs of harmonic 316L stainless steel samples after dynamic polarization to 0.8 V in 3.5% NaCl solution

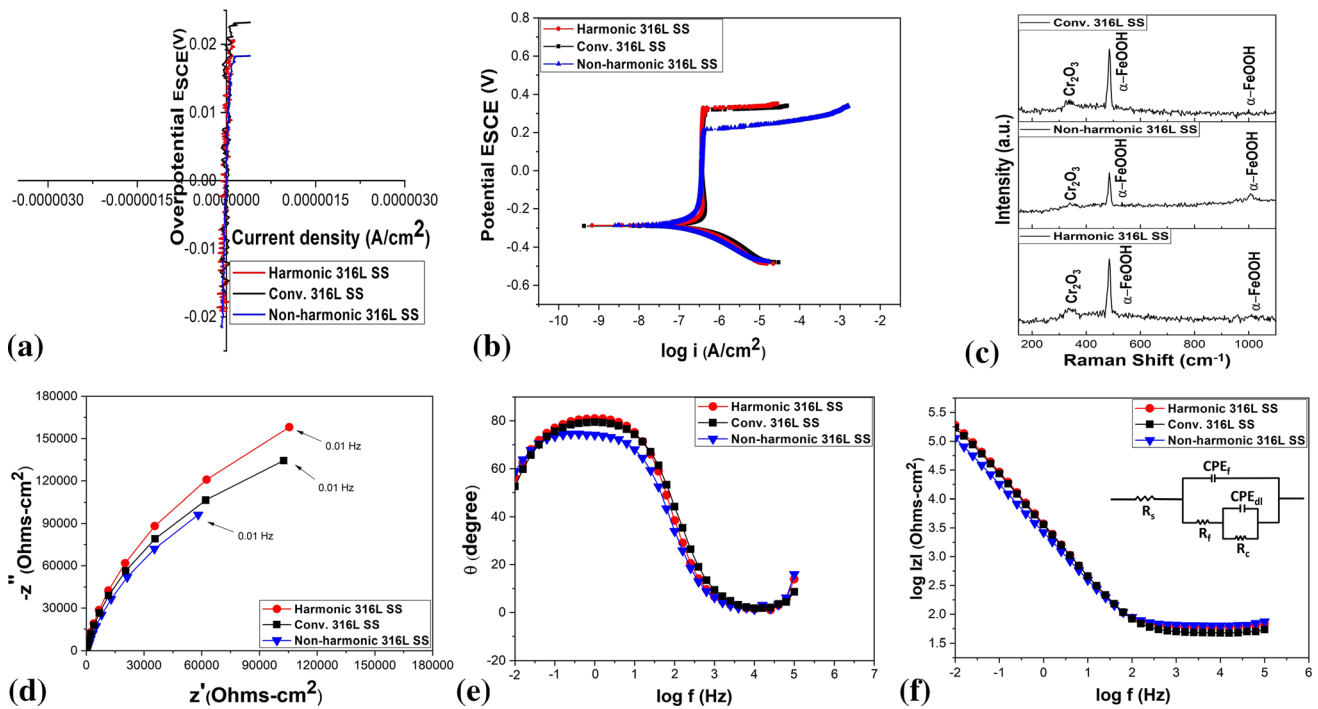


Fig. 9 (a) Linear polarization, (b) dynamic polarization, (c) Raman spectroscopy plot, (d) Nyquist plot, (e) bode phase angle plot and (f) Bode magnitude plot for harmonic, conventional and non-harmonic 316L stainless steel samples tested in Hanks' solution

similar corrosion behavior of the conventional and harmonic steels lies on the variation in HAGB length per unit area and twin length per unit area (Fig. 5a and b) as it has been discussed while describing the similar corrosion behavior of both the steels in 3.5% NaCl solution (Fig. 6).

The passive films formed over the surfaces of the harmonic, the non-harmonic and the conventional 316L stainless steels after dynamic polarization test in the Hanks' solution have been analyzed using Raman spectroscopy, and the data are shown in Fig. 9(c). The presence of Cr_2O_3 and $\alpha\text{-FeOOH}$ over the samples surface is confirmed (Ref 28–30). Since, both chromium oxide and $\alpha\text{-FeOOH}$ are passive in nature, the formation of passive film over the surfaces of the harmonic, non-harmonic and conventional 316L stainless steels is very much expected. However, the relative fractions of the Cr_2O_3

and $\alpha\text{-FeOOH}$ in the harmonic, conventional and non-harmonic steels have been calculated by comparing the area under the peaks of both the phases. They are 1.37:1.22:1.0 for the Cr_2O_3 phase and 1.17:1.21:1.0 for the $\alpha\text{-FeOOH}$ phase in the harmonic, conventional and non-harmonic steels. Hence, the passivation over the harmonic and conventional steels is expected to be stronger than that of the non-harmonic steel. The presence of other elements in the passive film could not be detected by Raman spectroscopy. Hence, the effect of the other elements on the passivity could not be analyzed.

Electrochemical impedance spectroscopy has also been performed in Hanks' solution for all three steels and modeled with the circuit shown in the inset of Fig. 9(f). Here also, the equivalent circuit is similar to the equivalent circuit used for fitting in case of impedance in NaCl solution for all the steels

Table 4 Values of electrochemical parameters obtained from electrochemical polarization in Hanks' solution

Material	$R_p, \Omega \text{ cm}^2$	$\beta_a, \text{mV/decade}$	$\beta_c, \text{mV/decade}$	$E_{\text{corr}}, \text{mV vs. SCE}$	$i_{\text{corr}}, \mu\text{A/cm}^2$
HS 316L SS	296934 ± 21536	6109 ± 53	103 ± 18	- 271 ± 16	0.036 ± 0.008
Conv. 316L SS	274177 ± 16274	5060 ± 27	104 ± 10	- 279 ± 09	0.039 ± 0.005
Non-HS 316L SS	305804 ± 13264	7931 ± 41	133 ± 13	- 301 ± 17	0.032 ± 0.006

Table 5 Data obtained from EIS measurements simulated using equivalent circuits in Hanks' simulated body fluid solution

Specimen condition	HS 316L SS	Conv. 316L SS	Non-HS 316L SS
$R_s, \Omega \text{ cm}^2$	52	56	48.4
$R_f, \Omega \text{ cm}^2$	35	45	55
$\text{CPE}_f, \Omega^{-1} \text{ s}^n \text{ cm}^{-2} \times 10^{-5}$	3.5	6.4	3.1
n_1	0.85	0.80	0.94
$R_c, \Omega \text{ cm}^2$	4.7×10^5	4.6×10^5	3.7×10^5
$\text{CPE}_{dl}, \Omega^{-1} \text{ s}^n \text{ cm}^{-2} \times 10^{-5}$	1.6	1.7	2.2
n_2	1.0	0.97	0.82
χ^2 (Chi-squared)	1.3×10^{-2}	1.4×10^{-2}	2.0×10^{-3}

because of the presence of strong passivation for all the steels in Hanks' solution. EIS data are listed in Table 5, and corresponding error in various parameters was found to be less than 8%. The Nyquist plots shown in Fig. 9(d) clearly indicate the highest polarization resistance of the harmonic 316L stainless steel among the three tested steels with different microstructures. Bode phase angle plots (Fig. 9e) also show capacitive response for the harmonic, conventional and sintered non-harmonic 316L steels. The EIS nature in NaCl as well Hanks' solution for the steels is somewhat similar. However, as compared to the steels in NaCl, the steels in Hanks' solution show capacitive behavior on wider frequency zone indicative of stabler passive zone in later solution (Fig. 9b). However, this is also visible in case of longer passive zone over much larger potential scan (Fig. 9b). The early breakpoint in polarization plots for the steel in NaCl is attributed to the lack of stronger passivation, whereas in Hanks' solution, oxidizing nature of the solution leads to stable passivity. It is reported in the literature that the presence of sulfate and phosphate ions together improves the corrosion resistance of iron in the solution of pH 7.2 (Ref 31). Bode magnitude plots (Fig. 9f) also corroborate the similar corrosion resistance of the harmonic, conventional and sintered non-harmonic 316L stainless steel samples.

The SEM micrographs of the exposed surface of all the three samples after dynamic polarization experiments in Hanks' solution are shown in Fig. 10(a), (b) and (c). It is clear that the samples of the harmonic, conventional and non-harmonic 316L stainless steel are not corroded significantly. Very small pits are observed in Fig. 10(a), (b) and (c) as shown with the arrow heads.

From the above experimental results and discussion, it is clear that even though the harmonic 316L stainless steel consists of fine and coarse grains and preferential dissolution of shell region occurs, the corrosion resistance of the harmonic 316L stainless steel has not degraded in either 3.5% NaCl or

Hanks' solution as compared to the wrought and sintered non-harmonic 316L stainless steels. Since grain boundaries are closely spaced and grain boundary area fraction in shell region is large, corrosion is preferentially localized in the fine-grained (shell) region leaving coarse-grained region un-corroded.

In this regard, it is important to indicate that the ratio of area fractions of the core (coarse region) and fine-grained shell region is ~ 1.56 since the area fractions of the coarse- and fine-grained regions are ~ 61 and 39% , respectively. Moreover, the fine-grained shell region has closely spaced HAGB, which would increase its free energy as compared to the core region. Therefore, there would be galvanic couple between the core and shell region, since higher free energy of the shell region would make it anodic as compared to the core region. Hence, the ratio between the area fractions of the core and shell regions (~ 1.56) would act unfavorably and shell region would corrode more. The present observation of greater degree of corrosion along the shell region (Fig. 8) supports this unfavorable area factor too. However, better mechanical (Ref 3, 9) and fretting wear properties (Ref 19, 20) of the harmonic steel than that of a conventional 316L steel are very exciting and if the area ratio of the shell and coarse grain regions can be equated to unity, the unfavorable area factor can be reduced to a great extent. It has already been shown that the 316L stainless steel with harmonic microstructure has resulted in good combination of hardness, strength and ductility. In this work, we show improved passivity and almost comparable corrosion resistance with that of conventional steel. This understanding, put together, make the harmonic structured 316L stainless steel useful, and it can be applied to various applications especially as a bio-implants. However, several other important tests, like detailed pitting resistance of harmonic steel as well as biocompatibility tests, are to be carried out before it could be actually used as bio-implant.

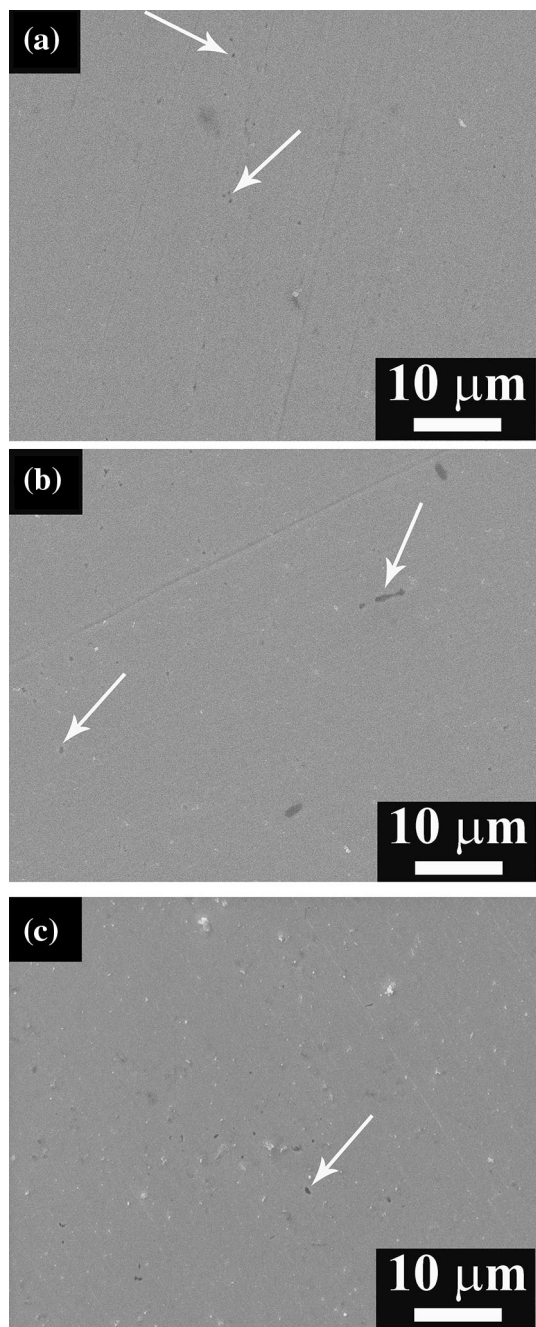


Fig. 10 SEM micrographs of (a) harmonic (b) conventional and (c) non-harmonic 316L stainless steel samples after dynamic polarization test in Hanks' solution

4. Conclusions

The harmonic structured 316L stainless steel has shown similar corrosion resistance to conventional and sintered non-harmonic 316L stainless steel in both 3.5% NaCl and Hanks' solution. The harmonic and conventional stainless steel samples have shown passivation tendency, whereas non-harmonic steel has not shown any signature of passivation. Moreover, harmonic structured 316L stainless steel has been found to have better passivation ability than the conventional and sintered non-harmonic 316L stainless steel in 3.5% NaCl

solution due to of the relatively larger HAGBs length/area and twin boundary length/area. Preferential dissolution of shell region occurs in case of the harmonic 316L stainless steel. Better mechanical properties of the harmonic steel coupled with comparable corrosion behavior with the conventional 316L stainless steel and stronger passivation of the harmonic steel are the salient outcome of this work.

Acknowledgment

Samples were prepared in the laboratory of Prof. K. Ameyama at Ritsumeikan University, Shiga, Japan, and it was supported by JSPS KAKENHI Grant No. JP18H05256.

References

1. G. Manivasagam, D. Dhinasekaran, and A. Rajamanickam, Biomedical Implants: Corrosion and its Prevention—A Review, *Recent Patents Corros. Sci.*, 2010, **2**, p 40–54
2. D. Bombač, M. Brojan, P. Fajfar, F. Kosel, and R. Turk, Review of Materials in Medical Applications, *RMZ Mater. Geoenviron.*, 2007, **54**, p 471–499
3. R. Zheng, Z. Zhang, M. Nakatani, M. Ota, X. Chen, C. Ma, and K. Ameyama, Enhanced Ductility in Harmonic Structure Designed SUS316L Produced by High Energy Ball Milling and Hot Isostatic Sintering, *Mater. Sci. Eng. A*, 2016, **674**, p 212–220
4. E.O. Hall, The Deformation and Ageing of Mild Steel: III, Discussion of Results, *Proc. Phys. Soc. Lond. Sect. B*, 1951, **64**, p 747–753
5. N.J. Petch, The Cleavage Strength of Polycrystals, *J. Iron Steel Inst.*, 1953, **174**, p 25–28
6. X.H. Chen, J. Lu, L. Lu, and K. Lu, Tensile Properties of a Nanocrystalline 316L Austenitic Stainless Steel, *Scr. Mater.*, 2005, **52**, p 1039–1044
7. H. Ueno, K. Kakihata, Y. Kaneko, S. Hashimoto, and A. Vinogradov, NANOSTRUCTURIZATION ASSISTED by Twinning During Equal Channel Angular Pressing of Metastable 316L Stainless Steel, *J. Mater. Sci.*, 2011, **46**, p 4276–4283
8. M. Eskandari, A. Najafzadeh, and A. Kermanpur, Effect of Strain-Induced Martensite on the Formation of Nanocrystalline 316L Stainless Steel After Cold Rolling and Annealing, *Mater. Sci. Eng. A*, 2009, **519**, p 46–50
9. K. Ameyama and H. Fujiwara, Creation of Harmonic Structure Materials with Outstanding Mechanical Properties, *Mater. Sci. Forum*, 2012, **706–709**, p 9–16
10. P.K. Rai, S. Shekhar, and K. Mondal, Development of Gradient Microstructure in Mild Steel and Grain Size Dependence of Its Electrochemical Response, *Corros. Sci.*, 2018, **138**, p 85–95
11. B.V. Mahesh and R.K.S. Raman, Role of Nanostructure in Electrochemical Corrosion and High Temperature Oxidation: A Review, *Metall. Mater. Trans. A*, 2014, **45**, p 5799–5822
12. K.T.A.R. Rofagha, R. Langer, A.M. El-Sheruk, U. Erb, and G. Palumbo, The Corrosion Behaviour of Nanocrystalline Nickel, *Scripta Metall. Mater.*, 1991, **25**, p 2867–2872
13. Y. Li, F. Wang, and G. Liu, Grain Size Effect on the Electrochemical Corrosion Behavior of Surface Nanocrystallized Low-Carbon Steel, *Corrosion*, 2004, **60**, p 891–896
14. D. Song, A. Ma, J. Jiang, P. Lin, and D. Yang, Corrosion Behavior of Ultra-Fine Grained Industrial Pure Al Fabricated by ECAP, *Trans. Nonferrous Met. Soc. China*, 2009, **19**, p 1065–1070
15. A. Balyanov, J. Kutnyakova, N.A. Amirhanova, V.V. Stolyarov, R.Z. Valiev, X.Z. Liao, Y.H. Zhao, Y.B. Jiang, H.F. Xu, T.C. Lowe, and Y.T. Zhu, Corrosion Resistance of Ultra Fine-Grained Ti, *Scr. Mater.*, 2004, **51**, p 225–229
16. A.Q. Lü, Y. Zhang, Y. Li, G. Liu, Q.H. Zang, and C.M. Liu, Effect of Nanocrystalline and Twin Boundaries on Corrosion Behavior of 316L Stainless Steel Using SMAT, *Acta Metall. Sin.*, 2006, **19**, p 183–189
17. G. Niu, H. Wu, D. Zhang, N. Gong, and D. Tang, Study on Microstructure and Properties of Bimodal Structured Ultrafine-Grained Ferrite Steel, *Metals*, 2017, **7**, p 1–13

18. P.K. Rai, S. Shekhar, M. Nakatani, M. Ota, S.K. Vajpai, K. Ameyama, and K. Mondal, Effect of Harmonic Microstructure on the Corrosion Behavior of sus304 l Austenitic Stainless Steel, *Metall. Mater. Trans. A*, 2016, **47**, p 6259–6269
19. P.K. Rai, S. Shekhar, M. Nakatani, M. Ota, S.K. Vajpai, K. Ameyama, and K. Mondal, Wear Behavior of Harmonic Structured 304 l Stainless, *J. Mater. Eng. Perform.*, 2017, **26**, p 2608–2618
20. P.K. Rai, S. Shekhar, K. Yagi, K. Ameyama, and K. Mondal, Fretting Wear Mechanism for Harmonic, Non-harmonic and Conventional 316L Stainless Steel, *Wear*, 2019, **424–425**, p 23–32
21. ASTM Standard G5-14, Standard reference test method for making potentiodynamic anodic polarization measurements, ASTM International, West Conshohocken, PA, (2014) <https://doi.org/10.1520/G0005-14>, www.astm.org
22. I. Gurappa, Characterization of Different Materials for Corrosion Resistance Under Simulated Body Fluid Conditions, *Mater. Charact.*, 2002, **49**, p 73–79
23. C. Sawangrat, S. Kato, D. Orlov, and K. Ameyama, Harmonic-Structured Copper: Performance and Proof of Fabrication Concept Based on Severe Plastic Deformation of Powders, *J. Mater. Sci.*, 2014, **49**, p 6579–6585
24. ASTM Standard G102-89, 2015e1, Standard Practice for Calculation of Corrosion Rates and Related Information from Electrochemical Measurements. ASTM International, West Conshohocken, PA (2015) <https://doi.org/10.1520/G0102-89R15E01>, www.astm.org
25. E.A. Trillo and L.E. Murr, Effect of Carbon Content, Deformation and Interfacial Energies on Carbide Precipitation and Corrosion Sensitisation in 304 Stainless Steel, *Acta. Mater.*, 1998, **47L**, p 235–245
26. T. Li, L. Liu, B. Zhang, Y. Li, F. Yan, and N. Tao, Passive Behavior of a Bulk Nanostructured 316L Austenitic Stainless Steel Consisting Of Nanometer-Sized Grains with Embedded Nano-Twin Bundles, *Corros. Sci.*, 2014, **85**, p 331–342
27. J. Yang, Y. Lu, Z. Guo, J. Gu, and C. Gu, Corrosion Behaviour of a Quenched and Partitioned Medium Carbon Steel in 3.5 wt% NaCl Solution, *Corros. Sci.*, 2018, **130**, p 64–75
28. D.A. Brown, D. Cunningham, and W.K. Glass, The Infrared and Raman Spectra of Chromium (III) Oxide, *Spectrochim. Acta*, 1967, **24**, p 965–968
29. S.J. Oh, D.C. Cook, and H.E. Townsend, Characterization of Iron Oxides Commonly Formed as Corrosion Products on Steel, *Hyperfine Interact.*, 1998, **112**, p 59–65
30. M. Mohammadtaheri, Q. Yang, Y. Li, and J. Corona-Gomez, The Effect of Deposition Parameters on the Structure and Mechanical Properties of Chromium Oxide Coatings Deposited by Reactive Magnetron Sputtering, *Coatings*, 2018, **8**, p 1–14
31. G. Kilinceker and B. Yazici, Effect of Phosphate (PO_4^{3-}) on the Corrosion of Iron in Sulphate Solution, *Turk. J. Chem.*, 1999, **23**, p 41–50

Publisher's Note Springer Nature remains neutral with regard to jurisdictional claims in published maps and institutional affiliations.